Journal of Materials Chemistry A

c5ta01251a

PAPER

A hybrid Si@FeSi$_y$/SiO$_x$ anode structure for high performance lithium-ion batteries *via* ammonia-assisted one-pot synthesis

Mingxia Gao, Dingsheng Wang, Xuqing Zhang, Hongge Pan,* Yongfeng Liu, Chu Liang, Congxiao Shang and Zhengxiao Guo

A hybrid micron/submicron-sized Si@FeSi$_y$/SiO$_x$ structure is developed by ball-milling of Si and Fe powders *via* ammonia-assisted one-pot synthesis. It shows superior electrochemical performance as an anode material for lithium-ion batteries.

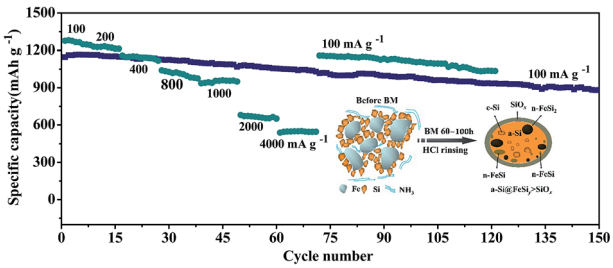

Please check this proof carefully. **Our staff will not read it in detail after you have returned it.**

Translation errors between word-processor files and typesetting systems can occur so the whole proof needs to be read. Please pay particular attention to: tabulated material; equations; numerical data; figures and graphics; and references. If you have not already indicated the corresponding author(s) please mark their name(s) with an asterisk. Please e-mail a list of corrections or the PDF with electronic notes attached - do not change the text within the PDF file or send a revised manuscript. Corrections at this stage should be minor and not involve extensive changes. All corrections must be sent at the same time.

Please bear in mind that minor layout improvements, e.g. in line breaking, table widths and graphic placement, are routinely applied to the final version.

We will publish articles on the web as soon as possible after receiving your corrections; **no late corrections will be made.**

Please return your **final** corrections, where possible within **48 hours** of receipt by e-mail to: materialsA@rsc.org

Queries for the attention of the authors

Journal: **Journal of Materials Chemistry A**

Paper: **c5ta01251a**

Title: **A hybrid Si@FeSi$_y$/SiO$_x$ anode structure for high performance lithium-ion batteries *via* ammonia-assisted one-pot synthesis**

Editor's queries are marked like this... **1**, and for your convenience line numbers are inserted like this... 5

Please ensure that all queries are answered when returning your proof corrections so that publication of your article is not delayed.

Query Reference	Query	Remarks
1	For your information: You can cite this article before you receive notification of the page numbers by using the following format: (authors), J. Mater. Chem. A, (year), DOI: 10.1039/c5ta01251a.	
2	Please carefully check the spelling of all author names. This is important for the correct indexing and future citation of your article. No late corrections can be made.	
3	The meaning of the sentence beginning "A suitable thickness…" is not clear - please clarify.	

Journal of Materials Chemistry A

PAPER

A hybrid Si@FeSi$_y$/SiO$_x$ anode structure for high performance lithium-ion batteries *via* ammonia-assisted one-pot synthesis†

Cite this: DOI: 10.1039/c5ta01251a

Mingxia Gao,[a] Dingsheng Wang,[ab] Xuqing Zhang,[a] Hongge Pan,*[a] Yongfeng Liu,[a] Chu Liang,[a] Congxiao Shang[c] and Zhengxiao Guo[d]

Received 15th February 2015
Accepted 12th April 2015

DOI: 10.1039/c5ta01251a

www.rsc.org/MaterialsA

Synthesised *via* planetary ball-milling of Si and Fe powders in an ammonia (NH_3) environment, a hybrid Si@FeSi$_y$/SiO$_x$ structure shows exceptional electrochemical properties for lithium-ion battery anodes, exhibiting a high initial capacity of 1150 mA h g^{-1} and a retention capacity of 880 mA h g^{-1} after 150 cycles at 100 mA g^{-1}; and a capacity of 560 mA h g^{-1} at 4000 mA g^{-1}. These are considerably high for carbon-free micro-/submicro-Si-based anodes. NH_3 gradually turns into N_2 and H_2 during the synthesis, which facilitates the formation of highly conductive FeSi$_y$ ($y = 1$, 2) phases, whereas such phases were not formed in an Ar atmosphere. Milling for 20–40 h leads to partial decomposition of NH_3 in the atmosphere, and a hybrid structure of a Si core of mixed nanocrystalline and amorphous Si domains, shelled by a relatively thick SiO$_x$ layer with embedded FeSi nanocrystallites. Milling for 60–100 h results in full decomposition of NH_3 and a hybrid structure of a much-refined Si-rich core surrounded by a mantle of a relatively low level of SiO$_x$ and a higher level of FeSi$_2$. The formation mechanisms of the SiO$_x$ and FeSi$_y$ phases are explored. The latter structure offers an optimum combination of the high capacity of a nanostructural Si core, relatively high electric conductivity of the FeSi$_y$ phase and high structural stability of a SiO$_x$ shell accommodating the volume change for high performance electrodes. The synthesis method is new and indispensable for the large-scale production of high-performance Si-based anode materials.

Introduction

With the increasing demand for Li-ion batteries in portable devices, electric vehicles, and stationary energy storage for grid integration of wind and solar energy, considerable effort has been devoted to the development of electrode materials with a high capacity and long lifetime. Silicon possesses a theoretical specific capacity of 3580 mA h g^{-1} at the highest accessible lithiation state of $Li_{15}Si_4$ at room temperature.[1] This is nearly ten times greater than that of commercialized graphite (372 mA h g^{-1}). However, commercial utilization of silicon is hindered by capacity deterioration due to its low electrical conductivity and huge volume expansion during lithiation, around tripling the volume when fully saturated, which causes severe pulverization of the silicon particles and eventual electrode failure.[2,3] Nano-sized Si,[4–6] and its porous structure[7] can viably decrease the overall volume change of Si during lithiation and delithiation, thus improving the cycle stability. However, most of those synthesis approaches are still not for large-scale production. Moreover, nano-sized and porous materials have low packing density, resulting in low volumetric density, which is also undesirable for practical applications. In addition, nanomaterials have large surface tension and readily agglomerate – hence lowering the electrochemical properties.

For a Si-based anode, both crystalline Si (c-Si) and amorphous Si (a-Si) are lithium reaction active. However, a-Si shows better pulverization resistance due to less volume expansion upon Li insertion.[8] Moreover, a-Si provides more pathways for lithium insertion/extraction compared with c-Si.[9,10] Pulverization of Si not only causes the loss of electronic contact of the particles, but also leads to the repeated formation of the solid electrolyte interface (SEI) layer on fresh surfaces,[5,11] both of which cause capacity fading. Coating functional layers, such as SiO$_x$,[12] TiO$_2$,[13] and AlF$_3$ (ref. 14) on the Si particle surface as a barrier can either prevent the direct exposure of Si to the electrolyte or/and buffer the volume expansion of Si during lithiation. Among those surface coated oxides, SiO$_x$ ($x \leq 2$) can form

[a]State Key Laboratory of Silicon Materials, Key Laboratory of Advanced Materials and Applications for Batteries of Zhejiang Province & School of Materials Science and Engineering, Zhejiang University, Hangzhou, 310027, P. R. China. E-mail: hgpan@zju.edu.cn; Fax: +86-571-87952615; Tel: +86-571-87952615

[b]Shanghai Electric Group Co., Ltd., Central Academe, Shanghai, 200070, P. R. China

[c]School of Environmental Science, University of East Anglia, Norwich, NR4 7TJ, UK

[d]Department of Chemistry, University College London, London, WC1H 0AJ, UK

† Electronic supplementary information (ESI) available: XRD, SEM, EDS and XPS results; mass spectra of the milling atmosphere of NH_3 after different periods of milling; differential capacity plots of the composites milled for 20, 80 and 100 h. See DOI: 10.1039/c5ta01251a

naturally on the surface of Si particles under an atmospheric environment, but the amount is limited due to its passivation effect. Bulk crystal SiO_2 is generally inactive for electrochemical lithium storage. However, nanostructured or amorphous SiO_2 is lithium reactive.[15,16] The theoretical specific capacity of SiO_2 is 1965 mA h g^{-1} when Li_2O and $Li_{22}Si_5$ are taken as the lithiation products.[17] SiO_x ($x < 2$) is commonly lithium reactive. They react with lithium, forming Si and Li_2O[18] or/and Li_4SiO_4,[19,20] in different mechanisms in the first lithiation process. The formed Li_2O and Li_4SiO_4 are commonly irreversible. However, those can serve as buffers to alleviate the volume expansion of Si in subsequent cycles. Therefore, SiO_x should theoretically demonstrate better cycle performance than Si.[21] SiO_x coated Si nanotubes were reported to have much better cycle performance than bare Si nanotubes because there was a much stable SEI layer formed at the surface of SiO_x compared with bare Si.[5] The reversible lithiation product of $Li_2Si_2O_5$ is reported in an amorphous SiO_2 film anode.[22] The amorphous SiO_2 is converted to $Li_2Si_2O_5$ and Si by lithium insertion. The capacity derived in this process is 357 mA h g^{-1}. The intermediate Si could be further lithiated,[21] and generated with more capacity.

The low electrical conductivity is another negative factor for Si to achieve a long cycle life and high-rate capability. For this reason, highly electrically conductive carbonaceous materials[23,24] and metal silicides, such as $FeSi_2$,[25] $TiSi_2$,[26] $TiFeSi_2$ (ref. 27) and $Ti_4Ni_4Si_7$ (ref. 28) were introduced to form Si/C and Si/metal silicide hybrid structures by different fabrication methods. The introduction of metal silicides not only improves the electronic conductivity of the Si-based anode, but also buffers partially the volume changes of Si during cycling as they are mostly inactive in the lithium reaction. As the mass density and tap density of metal silicides are high, the introduction of metal silicides is not expected to cause undue decrease in the volumetric capacity of the Si-based anodes. $FeSi_2$ alloy is of low cost compared with other metal silicides. Si/$FeSi_2$ hybrid structures are synthesized by high-energy ball milling of Fe and Si powders with excess Si,[25] and by high-energy ball milling of the industrial $FeSi_6$ alloy (*ca.* 25 wt% Fe and 75 wt% Si) in an Ar atmosphere.[29] However, the cycle stability of Si/$FeSi_2$ hybrid structures thus obtained is rather low. The Si/$FeSi_2$ hybrid structure prepared by the high-energy ball milling of Fe and Si powders only shows a capacity retention of 45% after 90 cycles.[25] Improved cycle stability is achieved only when graphite is further introduced by further planetary milling. The milled $FeSi_6$ alloy with 40 wt% of graphite shows a capacity of 615 mA h g^{-1} and capacity retention of 77% after 50 cycles.[29]

In this study, we developed new particulate Si@$FeSi_y$/SiO_x hybrid structures with nanocrystalline and amorphous Si core coated by a diphase layer of amorphous SiO_x and nanocrystalline $FeSi_y$ ($FeSi_2$ and FeSi) *via* "one-pot" planetary (low-energy) ball-milling of Si and Fe powders. It is identified that the formation of $FeSi_2$ alloys are largely facilitated even under low-energy milling by atmospheric NH_3, which further decomposes to N_2 and H_2 during milling, whereas they were not formed by the same milling process in an Ar atmosphere. The hybrid structures are in micron/submicron sizes and show superior electrochemical performance as anode materials for LIBs. The carbon-free and micron/submicron particles of the hybrid structures offer high packing density for the anodes. The method is facile and feasible for the large-scale production of high-performance Si-based anode materials for practical applications.

Experimental section

As-received Si (1–2 μm, >99.99%, Shanghai ST-Nano) and Fe (10−50 μm, Sinopharm, Shanghai) powder particles, without further purification, were ball-milled in an NH_3 atmosphere by a planetary mill (QM-1SP04, Nanjing, China). A weight ratio of Si : Fe = 2 : 1 was used. The oxygen content of the as-received Si measured using an oxygen analyzer (TC-436, LECO) is 5.6 wt%, which is believed to come from the oxidation layer of SiO_x on the Si particle surface formed naturally under an ambient atmosphere. The milling was performed for 20–100 h at a rotation speed of 500 rpm. A ball-to-powder ratio of 15 : 1 and a 6 bar NH_3 pressure were used. The milled products were then rinsed in a 10 wt% HCl solution to remove any residual Fe. The final hybrid structures were collected by centrifugal separation with deionized water several times and then dried at 120 °C in air for 10 h.

The microstructure of the hybrid structures was characterized by X-ray diffraction (XRD) (X'Pert PRO, PANalytical, Cu Kα radiation), field-emission scanning electron microscopy (FE-SEM, S-4800, Hitachi), energy dispersive spectrometry (FESEM-EDS), transmission electron microscopy (TEM, Tecnai G2 F30, FEI), high resolution TEM (HRTEM), and Raman techniques (Confocal Mirco-Raman Spectroscopy, inVia-Reflex, Renishaw plc, 514 nm wavelength incident laser light). X-ray photoelectron spectroscopy (XPS, ESCALAB 250Xi, Thermo Scientific, Al Kα X-ray radiation source, photon energy of 1486.6 eV) was used for the analysis of the chemical valence of Si in the material. The O content of the hybrid structures was also analyzed by the oxygen analyzer. To monitor the change of NH_3 during milling, the atmosphere was analyzed every 20 h of milling by mass spectrometry (MS, QIC-20, HIDEN).

The anodes were prepared by coating the slurry of the as-prepared hybrid structures (60 wt%), conductive agents (15 wt% acetylene black and 15 wt% vapor growth carbon fiber, VGCF) and sodium carboxymethyl cellulose (CMC, 10 wt%) as the binder, which are dispersed in a buffer solution of citric acid, NaOH and HCl with a pH value of 3, on a copper foil using a blade coater. The anodes were dried at 120 °C in vacuum and subsequently pressed at room temperature. The mass loading of the hybrid structure for each electrode was *ca.* 1 mg cm^{-2}. The use of the combined acetylene black and VGCF as conductive agents is in order to improve the electrochemical property of the anodes as VGCF has better electron conductivity than acetylene black. The previous study also showed that a combined carbon black and VGCF conductive agents provided a better cycling stability for a Si anode than a single carbon black conductive agent.[30]

2025 coin-type cells were assembled in an Ar-filled glove box (Labstar, Braun, Germany) with a lithium metal foil as the

counter electrode. A solution of 1 M $LiPF_6$ in a 1/1 (wt/wt) of ethylene carbonate (EC) and dimethyl carbonate (DMC) was used as the electrolyte. The cells were galvanostatically discharged (lithiated) and charged (delithiated) in a potential range of 0.02–1.5 V *vs.* Li^+/Li on a multi-channel battery testing system (Neware BTS-610, China) at a discharge/charge current of 100 mA g^{-1}. The rate capability of the hybrid structures was performed in a current range from 100 up to 4000 mA g^{-1} in the same potential range. All electrochemical tests were performed at 25 ± 1 °C.

To analyse the hybrid structures after cycling, selected samples after 5 cycles (full lithium extraction state cycled at 100 mA g^{-1}) were disassembled in the glove box, and then soaked in DMC for 2 h to remove lithium salts. The obtained products were ultrasonically treated for 30 min in ethanol and then performed by TEM and HRTEM observation. The thickness change and the surface morphology of a representative hybrid structure electrode after an initial lithiation with current of 100 mA g^{-1} are also observed by SEM.

For comparison, selected parallel tests were also performed for the pristine Si.

Results and discussion

Structural characterization

The XRD pattern of the starting mixture of Si and Fe powders is shown in Fig. S1 (ESI†). Both show a crystalline structure. Individual Fe was detected by XRD in the as-milled products after different periods of milling, indicating the existence of residual Fe. However, Fe is fully removed from the as-milled products after rinsing in the HCl solution. Fig. 1a shows the XRD patterns of the hybrid structures after removing the residual Fe as well as the pristine Si. It is seen that Si is the main crystal phase detected in the hybrid structures after 20–40 h of milling. In addition, a hump at *ca.* 22° is vaguely seen, especially in the hybrid structure after 40 h of milling, which is likely from amorphous SiO_x. The peaks of Si seem broadened with increasing the milling period up to 100 h. Calculation of the (111) Bragg peak of Si for the pristine Si and the Si in the hybrid structures using the Scherrer equation[31] shows that the crystallite size of the Si in the hybrid structures decreases after the milling, from *ca.* 51 nm of the pristine Si to 37–11 nm after milling for 20–100 h. The details are listed in Table S1.† The decrease in crystallite size demonstrates an increasing disorder of the Si structure in the hybrid structure with increasing milling time.

Further seen in Fig. 1a, a weak diffraction peak appears at *ca.* 45° in all the hybrid structures, which corresponds to the (110) facet of FeSi (JCPDS, no. 89-7376) and indicates the formation of trace FeSi. Moreover, diffraction peaks of $FeSi_2$ (JCPDS, no. 35-0822) are visibly seen in the hybrid structures after 60–100 h of milling, but are not evidence in those after 20–40 h of milling. It is inferred that Si reacted with Fe during the milling process, forming FeSi first and then $FeSi_2$. Raman measurement, Fig. 1b, further shows that the intrinsic peak of crystalline Si, which exists at *ca.* 520 cm^{-1}, broadens and shows a large extent of red shift with the increase of milling time. In addition, the broad peak centered at *ca.* 480 cm^{-1}, which is related to amorphous Si, shows a relatively high intensity for the hybrid structures milled for 60–100 h. The results are also consistent with that from the XRD analysis that Si tends to become much disordered with the increase of the milling time.

As an overall observation by SEM, the morphology and particle size distribution of the hybrid structures are not visibly changed during the 20–100 h milling. Typical SEM morphologies of the hybrid structures are shown in Fig. 2a and b from those after 20 and 100 h of milling, respectively. The particles are well dispersed in micron and sub-micron sizes with irregular shapes. The size of the hybrid structures is considerably reduced compared with those of the pristine Si and Fe powders shown in Fig. 2c and d, respectively.

There is also no distinguishable difference in the morphology of the hybrid structures milled for different periods of time, observed by normal TEM. A representative TEM image of the hybrid structures, after 40 h of milling, is shown in Fig. S2.† Particles of submicron sizes are observed. However, detailed information about the structures of Si, FeSi and $FeSi_2$ phases in the hybrid structures is shown by HRTEM, *e.g.* in Fig. 3a, for the sample milled for 40 h. Clearly, the crystalline structure of Si was greatly modified after milling, compared

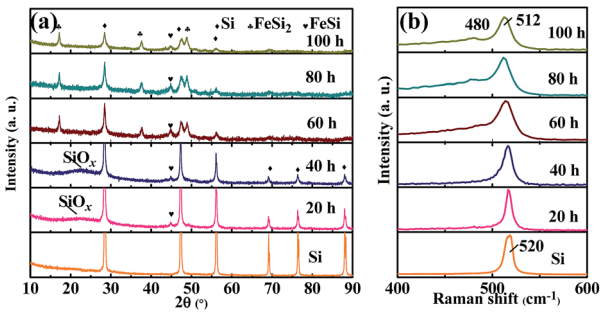

Fig. 1 XRD patterns (a) and Raman spectra (b) of the composites obtained by milling Si and Fe powders in NH_3 for different hours as well as the pristine Si.

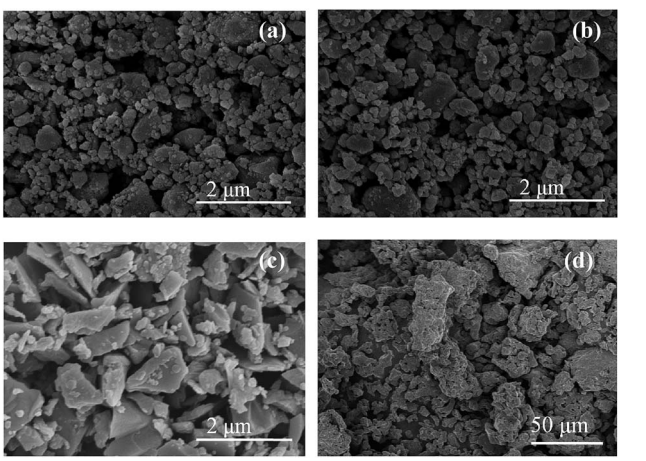

Fig. 2 SEM images of the composites after 20 h (a), 100 h (b) of milling, and the starting Si (c) and Fe (d) powders.

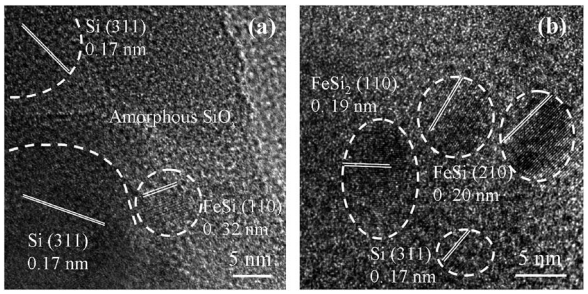

Fig. 3 HRTEM images of the composites after 40 h (a) and 60 h (b) of milling.

with the pristine Si shown in Fig. S3,† where a highly ordered lattice and a very thin amorphous surface layer, which is supposed to be SiO_x, are observed. Though the Si lattice is still observed in Fig. 3a, as noted from the lattice fringe of 0.19 nm, corresponding to the *d* spacing of the Si (220) facet, the lattice is rich in defects. Moreover, there is an unevenly much thicker amorphous layer on the surface of the Si particles, which should mainly be SiO_x. The FeSi nanocrystallite is found embedded in the amorphous matrix. For the hybrid structure milled for 60 h, Fig. 3b, the crystalline Si structure is mostly damaged, where nanocrystallites of both $FeSi_2$ and FeSi phases are embedded in an amorphous matrix. Though crystalline Si domains still exist, as marked in Fig. 3b, the domains are much smaller in size and in number than those in the 40 h-milled one. The much-disordered structure of Si after prolonged milling is also consistent with the findings from XRD and Raman spectra analyses.

The results of the XPS analysis of the chemical valance states of Si in the hybrid structures and the pristine Si are shown in Fig. S4a–f.† The visible peaks centered at *ca.* 103 eV with a broad shoulder can be assigned to SiO (102.4 eV) and SiO_2 (103.2 eV), which confirm the presence of a SiO_x layer on the particle surfaces. The small peak centered at *ca.* 99 eV corresponds to Si $2p_{3/2}$ (99.0 eV) and Si $2p_{1/2}$ (99.6 eV). This signal of Si^0 could be from the individual Si domains in the SiO_x layer or/and the Si matrix under the SiO_x layer. By integration of the peak intensities, the atomic percentages of Si^0, Si^{2+} and Si^{4+} in the detected surface layers are obtained and listed in Table S2.† Assuming that the SiO_x layer only consists of homogenously mixed SiO_2 and SiO, with the detected ratio by XPS, we can estimate the *x* value of SiO_x for the hybrid structures. The result is also listed in Table S2.† The *x* value of SiO_x in the pristine Si is estimated to be 1.7, and it decreases to about 1.5 for the hybrid structures after different periods of milling, indicating that an almost identical SiO_x structure is formed in the hybrid structures.

The elemental compositions of the hybrid structures detected by EDS under SEM are listed in Table S3.† Given a higher precision for O measurement by an oxygen analyzer than the EDS, the O content of the hybrid structures was also determined by the oxygen analyzer, the results of which are also listed in Table S3.† It is noted that the O content detected by EDS is slightly different from that by the oxygen analyzer. Thereby, the Si and Fe contents of the hybrid structures are rectified by assuming that the ratios of Si to Fe are the same as those obtained by EDS, and the O content of the hybrid structures is taken as that obtained by the oxygen analyzer. The rectified values of the Fe and Si concentrations are also listed in Table S3.† The high O contents (measured using the oxygen analyzer LECO) of 19.0 and 26.7 wt% for the hybrid structures milled for 20 and 40 h, respectively, and their low Fe content of 3.3 wt% demonstrate a high level of SiO_x and a low level of FeSi. However, the O content in the hybrid structures milled up to 60–100 h is significantly decreased to 6.2–8.5 wt%, and the Fe content is remarkably increased to *ca.* 20 wt%, indicating a low level of SiO_x but a high level of Fe–Si phases.

The phase ratios of the hybrid structures are further estimated as follows. By means of the *x* value of SiO_x (Table S2†) and the O content in the hybrid structures detected by the oxygen analyzer (Table S3†), the SiO_x content of the hybrid structures is estimated and listed in Table 1. The undetectable diffraction signal from SiO_x in the pristine Si and the hybrid structures milled for 60–100 h by XRD (Fig. 1a) is supposed to be due to their extremely poor crystallinity and comparatively lower level than those in the structures milled for 20–40 h. As only FeSi is detected by XRD in the hybrid structures milled for 20 and 40 h, the Fe content in the two hybrid structures may be assumed to be from FeSi, and hence the content of FeSi in the two hybrid structures is estimated and also listed in Table 1. The FeSi in the two hybrid structures is only of *ca.* 5.0 wt%. As the relative peak intensity of FeSi in the hybrid structures milled for 60–100 h is also as low as those in the ones milled for 20–40 h, we may roughly assume that the FeSi in these hybrid structures is also 5.0 wt%, and thus the other Fe content must be from $FeSi_2$. Hence, the content of $FeSi_2$ in the hybrid structures milled for 60–100 h can be estimated to be in the range of 32–35.4 wt%, as listed in Table 1. The result is also consistent with the high relative peak intensity of $FeSi_2$ in their XRD patterns. The Si content of the hybrid structures listed in Table 1 is obtained by the subtraction of those of SiO_x, the FeSi and $FeSi_2$ phases. In addition, as the content of SiO_x in the 60 h-milled hybrid structure is much lower than that in the 40 h-milled, it is demonstrated that the amorphous matrix in Fig. 3b consists of not only SiO_x, but also amorphous Si.

As seen from Table 1, the content of SiO_x is evidently increased in the hybrid structures compared with the pristine Si, especially for those milled for 20–40 h. Increase of SiO_x in milled Si was also found in our previous work[32] and other report.[33] One of the possible reasons is that milling creates considerable fresh surfaces and surface defects on Si particles,

Table 1 Phase compositions of the pristine Si and the composites after different periods of ball milling (wt%)

Samples		Si	SiO_x	FeSi	$FeSi_2$
Pristine Si		88.6	11.4	–	–
Si@$FeSi_y$/SiO_x	20 h	53.7	41.3	5.0	–
	40 h	36.2	58.8	5.0	–
	60 h	49.5	13.5	5.0	32.0
	80 h	44.4	15.8	5.0	34.8
	100 h	41.2	18.4	5.0	35.4

which facilitate the formation of SiO_x by reaction with oxygen in the ambient atmosphere once the samples are taken out from the milling jar. The higher content of SiO_x in the hybrid structures milled for 20–40 h than those milled for 60–100 h is attributed partially to the high content $FeSi_2$ phase in the latter that anchored possibly on the surface of the Si core since $FeSi_2$ is much ductile than Si as also supposed in the ball-milling of a $Si/FeSi_2$ system,[25] which results in reduced exposure of "free" Si surfaces and hence reduces the formation of SiO_x. However, the difference between the amounts of SiO_x and Fe–Si phases is extremely large for the hybrid structures milled for 20–40 h and for 60–100 h. It seems that 40 h is the critical milling period to create the largest difference.

In order to clarify the dramatic structural change of the hybrid structures upon milling for the periods of 20–40 h to 60–100 h, the composition of the milling atmosphere was analyzed by MS (Fig. S5†). The result shows that NH_3 was partially decomposed to N_2 and H_2 up to 20–40 h of milling, but fully decomposed after milling for 60 h. The decomposition of NH_3 is likely attributed to the mechanical milling energy. Perrine *et al.*[34] report that a clean and fresh Si surface could be terminated with H^+ and NH^{2-} groups while fresh Si was exposed to ammonia in an ultrahigh vacuum chamber at room temperature. In addition, Chirvony *et al.*[35] show that H-terminated Si particles can react with H_2O, forming terminal hydroxides, into which H_2O can further penetrate and the Si–Si bonds are inserted by oxygen, forming silicon oxide. That Si particles terminated weakly with H^+ may be possible in the hybrid structures after 20 and 40 h of milling, due to the decomposition of NH_3 and the generation of a fresh surface of Si during milling. Therefore, extra SiO_x is generated in the hybrid structures milled for 20–40 h after the as-milled products were rinsed in the HCl solution and deionized water. When the milling time is greater than 60 h, as NH_3 has been fully decomposed to N_2 and H_2 (Fig. S5†), the earlier formed weak H^+ terminals is damaged upon further milling, which hinders the extra formation of SiO_x during the rinsing process, resulting in the low amount of SiO_x. The O measurement of the as-milled products without being rinsed in HCl solution to remove the residual Fe show O contents of 9.6 and 6.5 wt% after 40 and 80 h of milling, respectively, which are much lower than those after rinsing in HCl. Even considering that the residual Fe in the former is higher than the latter, the difference of the O contents between the two hybrid structures is not as significant as that in the $Si@FeSi_y/SiO_x$ hybrid structures rinsed in HCl solution. This phenomenon also indicates that it is likely that a considerable amount of SiO_x in the hybrid structures milled for 20–40 h was generated during the rinsing process.

To further clarify the formation mechanism of $FeSi_2$, another experiment was conducted by milling the same ratio of Si and Fe powder particles in four different atmospheric environments (with the same pressure and other milling parameters as used for the atmosphere of NH_3): (1) in NH_3 for 40 h followed by another milling in a mixed gas atmosphere of N_2 and H_2 (1/3 by v/v) for 20 h, simulating the variation of the milling atmosphere of NH_3 during the 60 h of milling; (2) in NH_3 for 40 h followed by another milling in fresh NH_3 for 20 h, preserving the atmospheric environment to be mainly NH_3; (3) in a mixed gas atmosphere of N_2 and H_2 (1/3 by V/V) for 60 h, simulating the fully decomposed atmosphere of NH_3; (4) in Ar for 60 h, an inert atmosphere. The XRD patterns of these as-milled products without or with residual Fe removed by rinsing in HCl solution are also shown in Fig. S1.† The results show that a large amount of $FeSi_2$ and a small amount of FeSi are formed with a part of the Si remaining under the first condition; there are almost no $FeSi_2$ and only a minor amount of FeSi, with a majority of Si and Fe remaining under the second condition; there is a large amount of $FeSi_2$ with highly disordered Si (as the diffraction peak intensity of Si is extremely weak) under the third condition; and there are only Si and Fe without any evidence of Fe–Si alloys under the fourth condition. The results demonstrate that the atmosphere of the decomposed products of NH_3 during milling, N_2 and H_2, facilitates greatly the formation of $FeSi_2$.

To further explore the essential factor for the formation of the $FeSi_2$ phase, the Fe powder was milled in NH_3 and Ar for 60 h, respectively. XRD analysis shows that the Fe powder is substantially disordered after milling in NH_3, whereas the one milled in Ar maintains mainly crystal structure, as shown also in Fig. S1†. In addition, elemental analysis of the Fe powder milled in NH_3 shows that the one milled in NH_3 contains 2.9 wt% of N, whereas there is no N detected in the one milled in Ar. EDS analysis under SEM (Fig. S6†) also shows that N penetrated into the Fe powder during milling in NH_3, whereas there was no signal of N detected in the one milled in Ar. When the two pre-milled Fe powders were further milled with Si in Ar for 60 h, respectively, it is interestingly found that a large amount of $FeSi_2$ and a small amount of FeSi are formed in the milled product from Fe pre-milled in NH_3, whereas there is almost no $FeSi_2$ formed in the milled product from Fe pre-milled in Ar. The XRD patterns of the two products are also shown in Fig. S1.† It is thus concluded that the damaged crystal structure of Fe associated with the penetration of N in the Fe particles should play an important role in the formation of the $FeSi_2$ phase.

Fig. 4 depicts schematically the fabrication process of the $Si@FeSi_y/SiO_x$ hybrid structures by milling in NH_3. The hybrid structures can be classified into two typical structures. During

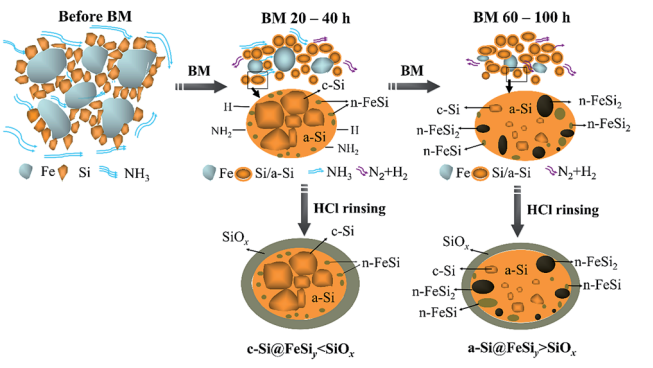

Fig. 4 Schematic illustration of the fabrication process of the $Si@FeSi_y/SiO_x$ hybrid structures (n-: nanocrystallite, c-: crystal, a-: amorphous).

the initial milling between 20 and 40 h, corresponding to the incomplete decomposition of NH_3, the hybrid structures show a structure of mixed amorphous and crystalline Si core coated with a thick amorphous SiO_x layer embedded with a few FeSi nanocrystallites. Those milled for 60–100 h, corresponding to the complete decomposition of NH_3, show a much-disordered Si core coated by a reduced SiO_x layer but with a large number of $FeSi_2$ and a small number of FeSi nanocrystallites dispersed in both the amorphous Si core and the SiO_x mantle.

Electrochemical performance

The voltage profiles at 100 mA g^{-1} of the Si@$FeSi_y$/SiO_x hybrid structures milled for different periods of time, as well as the pristine Si, are shown in Fig. 5. The considerably flat plateau corresponds mostly to the lithiation of Si. The initial discharge/charge capacities, irreversible capacities and Coulombic efficiencies are listed in Table 2. As expected, pristine Si shows the highest initial discharge/charge capacities of 3730/2950 mA h g^{-1}, corresponding to an initial Coulombic efficiency of 79%. As an overview from Table 2, the initial reversible capacity of the hybrid structure decreases with the increase of milling time, which are likely due to the decreased Si content (Table 1).

The initial irreversible capacity of the hybrid structure and pristine Si is from both the commonly irreversible SEI formation and also the irreversible reaction of SiO_x with lithium. The higher initial Coulombic efficiency of the pristine Si than those of the hybrid structures (Table 2) is likely due to its larger particle size for less SEI formation and its lower amount of SiO_x. The hybrid structures milled for 20 and 40 h show comparatively lower initial Coulombic efficiencies than those milled for 60–100 h, mainly due to their higher SiO_x contents. The slightly higher SiO_x content is also the reason for the slightly lower initial Coulombic efficiency of 59% of the sample milled for 40 h than that of 63% of the one milled for 20 h. Similar values of initial Coulombic efficiency (67–69%) are obtained for those milled for 60–100 h (Table 2), due to their comparable structures. The low initial Coulombic efficiency of the Si@$FeSi_y$/SiO_x hybrid structures is likely due to the irreversible lithiation product of SiO_x formed in the initial lithiation, such as Li_2O or/and Li_4SiO_4.[18–20] If ways can be found out to change the lithiation product to a reversible one, such as $Li_2Si_2O_5$,[22] or to improve the reversibility of Li_2O and Li_4SiO_4, the initial Coulombic efficiency of the hybrid structures is hopefully improved.

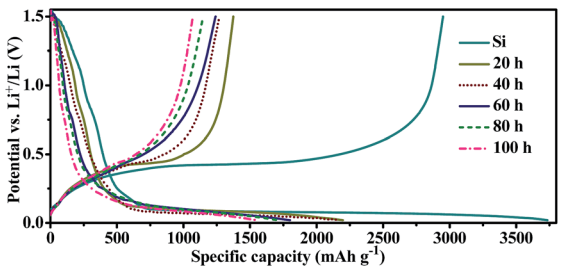

Fig. 5 Voltage profiles of the Si@$FeSi_y$/SiO_x hybrid structures and of pristine Si (100 mA g^{-1}).

Fig. 5 further shows that the slope of the sloping discharge plateau in the high potential range increases with milling time, corresponding to a smaller discharge capacity. This means a decreasing irreversible capacity generated from the reactions of the electrode and the electrolyte, and the SEI formation, which is likely due to the decreasing amount of the total lithium-active materials of Si and SiO_x. In addition, as a higher content of SiO_x causes a higher initial irreversible capacity from the formation of irreversible lithium oxide and/or lithium silicides, the irreversible capacities of the hybrid structures milled for 20–40 h are higher than those milled for 60–100 h (Table 2).

Amorphous SiO_x can be considered as consisting of tiny domains of SiO and SiO_2. Previous studies on analyses of the differential capacity plots (DCPs) shows that the lithiation of SiO or amorphous SiO_2 to form Li_4SiO_4 or Li_2O takes place around 0.24–0.25 V (*vs.* Li^+/Li).[16,19,36] In addition, a slightly lower potential of 0.14 V is reported for the formation of Li_4SiO_4 in the lithiation process of a SiO anode material modified by surface etching and heat treatment,[37] while a value of 0.2 V is reported in a SiO anode prepared by high-energy ball milling.[38] In addition, the formation of $Li_2Si_2O_5$ in the lithiation product of a hollow porous SiO_2 nanocube discharged up to 0 V was also proposed, but there was no distinguishable reaction peak found in the cyclic voltammetry curve.[17] Formation of $Li_2Si_2O_5$ at 0.55 V and subsequently Li_4SiO_4 at 0.14 V (from DCPs) is also reported for the SiO anode.[37]

Fig. 6a–c shows typically the DCPs of the pristine Si, the hybrid structure with a high level of SiO_x but a low level of FeSi (40 h of milling), and the one with a low level of SiO_x but a high level of $FeSi_2$ (60 h of milling). Those with 20, 80 and 100 h of milling are shown in Fig. S7.† As seen from Fig. 6 and S7,† all the hybrid structures and also the pristine Si show only one

Table 2 Electrochemical property at 100 mA g^{-1} of the Si@$FeSi_y$/SiO_x hybrid structures and of pristine Si

Samples		1st discharge capacity (mAh g^{-1})	1st charge capacity (mAh g^{-1})	1st coulombic efficiency (%)	1st irreversible capacity (mAh g^{-1})	150th capacity (mA h g^{-1})	Capacity retention after 150 cycles (%)
Pristine Si		3730	2950	79	780	440	15
Si@$FeSi_y$/SiO_x	20 h	2190	1370	63	820	730	53
	40 h	2170	1280	59	890	780	61
	60 h	1810	1250	69	560	820	66
	80 h	1710	1150	67	560	880	77
	100 h	1540	1070	69	470	820	77

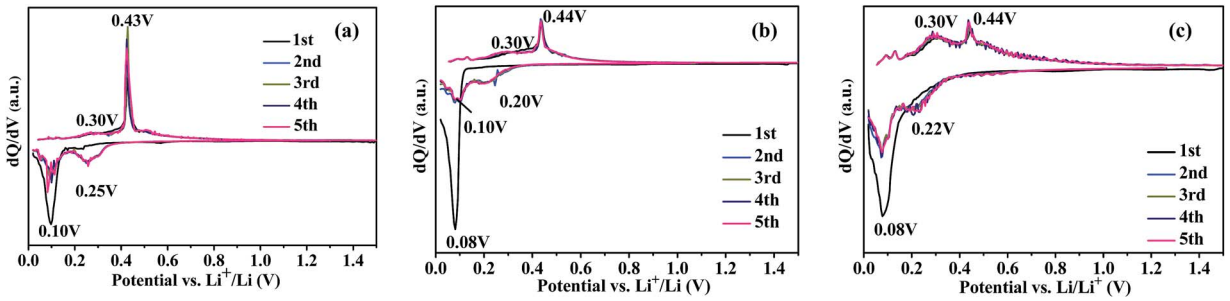

Fig. 6 Differential capacity plots (DCPs) of the pristine Si (a), the hybrid structures milled for 40 h (b) and 60 h (c) for the first 5 cycles.

sharp cathodic peak centered at *ca.* 0.1 V in the first sweep. There is no visible cathodic peak above 0.2 V in the present study, which is very different from the above reported lithiation process of SiO_x, occurring at potentials higher than 0.2 V. A possible reason is that the present SiO_x lithiated at a potential lower than 0.2 V, which is overlapped by the large peak centered at *ca.* 0.1 V, where the lithiation of Si takes place. The peak centered at *ca.* 0.1 V is significantly reduced after the first cycle, demonstrating an irreversible reduction. Further from Fig. 5, we note that the capacity generated from the sloping discharge plateau at a potential higher than 0.2 V is smaller than the initial irreversible capacity as shown in Table 2. As the sloping plateau is generally attributed to the irreversible reaction between the electrode and the electrolyte, and the decomposition of the electrolyte,[17] it is reasonable to assume that the lithiation of SiO_x takes place at a potential lower than 0.2 V. In addition, a new anodic peak centered at *ca.* 0.22 V occurs after the second cycle for all the hybrid structures, which is mainly attributed to the lithiation of amorphous Si to form amorphous Li_xSi phases according to previous studies.[39,40] The higher potential for the dominated lithiation of Si after the second cycle is due to the change in structure, morphology, as well as electronic contact of Si.

Moreover, as seen from Fig. 6 and S7,† there is almost one anodic peak located at *ca.* 0.44 V for the hybrid structures milled for 20–40 h, in addition to a vague hump around 0.30 V, whereas there are two visible anodic peaks located at *ca.* 0.30 and 0.44 V for those milled for 60–100 h. Along with the microstructures of the hybrid structures, it is inferred that the high level of the highly conductive $FeSi_2$ phase and the much disordered structure of Si facilitate lithium extraction starting considerably at a relatively low potential, improving the reaction kinetics. Similar potential values for lithium extraction are also reported by Obrovac *et al.*[1] in an amorphous Si electrode. The similar microstructure in the group of 20–40 h and of 60–100 h milling results in the similar DCPs in each of them, as seen from Fig. 6 and S7.† The redox peaks of the hybrid structures are well repeated after the second cycle, indicating a high cycle stability. In addition, the slightly lower lithiation potential of 0.20 V and the slightly higher delithiation potential of 0.44 V for the hybrid structures milled for 20–40 h than those of 0.25 and 0.42 V for pristine Si, respectively, are likely due to the higher content of inactive Li_2O or/and lithium silicides generated in the former, which block the diffusion of Li ions between the electrolyte and the Si particles.

Further seen from Fig. 6 and S7,† for the hybrid structures milled for 20–40 h and the pristine Si, the evident initial lithium insertion starts at a potential lower than 0.2 V. However, for the hybrid structures milled for 60–100 h, the evident initial lithium insertion starts at a potential around 0.4 V, which is much higher than the former. As the SiO_x content in the former is much higher than the latter, it is likely that lithium insertion at the high potential is not from the lithiation of SiO_x, or at least, not only from the lithiation of SiO_x. Much likely, the high level of the highly electron conductive phase of $FeSi_2$ and the much disordered structure of Si induce the lithiation of Si or possibly also SiO_x to take place at a relatively high potential.

Fig. 7a shows the cyclic performance of the Si@$FeSi_y$/SiO_x hybrid structures milled for different periods at 100 mA g^{-1}, with that of the pristine Si shown as the inset for comparison. The capacities and the capacity retentions of the hybrid structures and the pristine Si after 150 cycles are also listed in Table 2. Though the initial reversible capacity of the pristine Si is high, after 150 cycles, its capacity is only 440 mA h g^{-1}, corresponding to a capacity retention of only 15%, whereas the

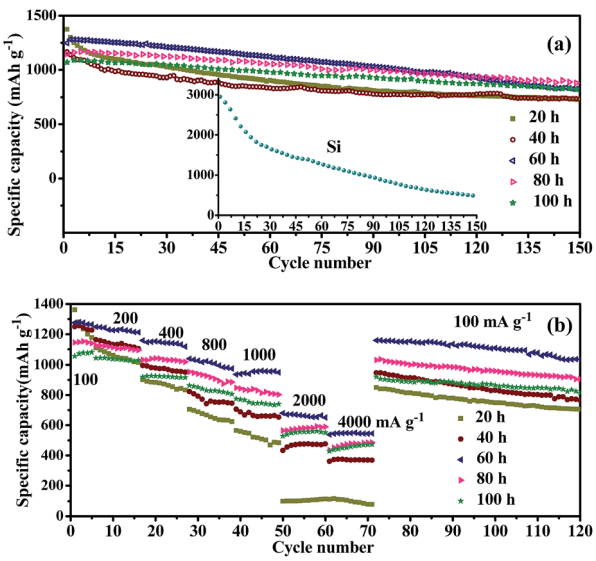

Fig. 7 Cycling performance at 100 mA g^{-1} (a) and rate capability (b) of the Si@$FeSi_y$/SiO_x hybrid structures milled for different periods.

capacities of the hybrid structures are in the range of 730–880 mA h g^{-1} after 150 cycles, corresponding to capacity retentions of 53–77%, which are all much higher than those of the pristine Si.

The Si in the hybrid structures milled for 20–40 h is partially disordered, therefore, its volume expansion during lithiation is less than that of pristine Si. Moreover, the high content of SiO_x (41–59 wt%) generates high content of irreversible Li_2O or/and Li_4SiO_4, serving as a buffer to alleviate the volume expansion of Si. In addition, the highly conductive phase of FeSi improves the electronic contact of the Si particles. All the above favour the cycle stability of the hybrid structures. For the hybrid structures milled for 60–100 h, although the formation of $FeSi_2$ and FeSi phases sacrifices some capacities, their roles in improving the electron conductivity of the anode and accommodating the volume change of Si during cycling lead to much higher capacity and capacity retention. Especially for the hybrid structure milled for 80 h, it possesses the highest capacity of 880 mA h g^{-1} after 150 cycles, corresponding to the capacity retention of 77%. With further increasing the milling time up to 100 h, the capacity retention is still 77%. However, due to its slightly lower content of active Si, both the initial reversible capacity and the capacity after 150 cycles are slightly lowered. Meanwhile, the hybrid structure with relatively shorter milling time of 60 h shows lower capacity (820 mA h g^{-1}) and capacity retention (66%) after 150 cycles than the one milled for 80 h; this is mainly due to the less disordered Si and possibly the slightly lower amounts of $FeSi_2$ and SiO_x phases.

The rate capability of the hybrid structures up to 4000 mA g^{-1} is shown in Fig. 7b. The hybrid structures milled for 60–100 h always show better high-rate capability than those milled for 20–40 h, which is attributed to the sufficiently high electronic conductive $FeSi_2$ phase, the much disordered structure of Si and the low level of SiO_x. Among those, the hybrid structure milled for 60 h shows the best rate performance, *e.g.* with a capacity of 560 mA h g^{-1} at 4000 mA g^{-1}, which is probably due to its slightly lower contents of $FeSi_2$ and SiO_x than those milled for 80 and 100 h. As $FeSi_2$ and the initial lithiation products of SiO_x, Li_2O and Li_4SiO_4 are lithium-reaction inactive, too much of those may hinder lithium transfer. In addition, Fig. 7b, all of the Si@$FeSi_y$/SiO_x hybrid structures show good capacity recovery while the rate is returned to 100 mA g^{-1} after cycling up to 4000 mA g^{-1}.

Although the results of the electrochemical properties from different research groups cannot be quantitatively compared due to different electrode preparation and testing conditions, it is still useful to review the progress in Si-based anode materials of micro/submicro-size made among the recent reports. A $FeSi_2$/Si hybrid structure with 50 wt% Si and comparable particle sizes of micron and submicron to our present ones prepared by high-energy ball milling of Fe and Si powders in an Ar atmosphere shows an initial capacity of 1287 mA h g^{-1} and a retention capacity less than 600 mA h g^{-1} after 90 cycles, corresponding to the capacity retention of 45%, at a discharge/charge current of 100 mA g^{-1},[25] which are all lower than the present ones. An enhanced capacity retention was obtained when the $FeSi_2$/Si hybrid structure was combined with 10 wt% graphite by further planetary milling, *e.g.* with an initial capacity of *ca.* 1010 mA h g^{-1} and capacity retention of 94% after 200 cycles at 100 mA g^{-1}.[25] However, the $FeSi_2$/Si@C hybrid structure shows inferior rate-capability in their tested current range of 200–1000 mA g^{-1}, compared with the present hybrid structures milled for 60–80 h. The capacity and capacity retention of the present hybrid structures are also superior to a micro-sized Si/Ni hybrid structure with a micro-Ni core with Si nanoparticles welded on the surface by rapid heat treatment, where an initial capacity of 650 mA h g^{-1} and a retention of 73% were obtained after 100 cycles at a current density of 233 mA g^{-1}.[41] Porous micro-sized Si with nanowire configuration on the surface, prepared by a multi-step method combining metal deposition, metal-assisted chemical etching and further coating by a carbon layer of 15 wt% by CVD, shows an initial reversible capacity of 2400 mA h g^{-1} at 0.1 C, and the capacity retention after 70 cycles was 95% at a rate of 0.2 C after pre-cycling at 0.1 C.[42] However, without carbon coating, though this multi-structured Si shows an initial reversible capacity of 1490 mA h g^{-1}, the capacity fading is rapid. The remaining capacity after 20 cycles is less than 400 mA h g^{-1} (0.1 C).[42]

The microstructure of the hybrid structures after 5 cycles in a full lithium extraction state was further analyzed by HRTEM. Fig. 8a and b shows representatively the HRTEM images, originally from those milled for 40 and 60 h, respectively. It is seen that all the initial Si particles, including the crystalline and the amorphous domains, become amorphous after cycling, while the $FeSi_2$ and FeSi phases retain their crystalline structures, indicating their stable structure during cycling (Fig. 8b). The thickness change of a representative hybrid structure electrode after an initial lithiation, which is from the 60 h-milled one, is shown in Fig. S8.† It is seen that the increase in thickness is less than 15% after the initial lithiation. The electrode after the initial lithiation also shows a mostly intact surface, as shown in Fig. S9a.† In comparison, the pristine Si electrode shows severe exfoliation after the initial lithiation, the surface morphology of which is shown in Fig. S9b.† Due to the severe exfoliation during the disassembling of the electrode from the cell, the thickness change of the pristine Si electrode after the initial lithiation was failed to be exactly estimated. A suitable thickness of SiO_2 coating on a kind of core@shell bulk@nanowire silicon particles is also reported greatly reduced the electrode thickness

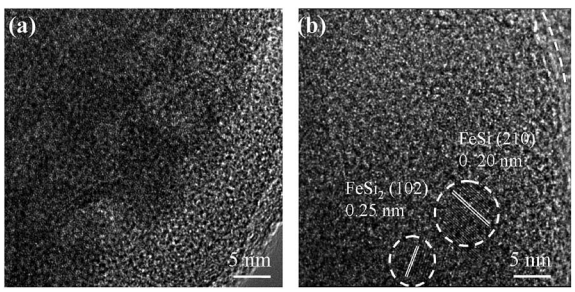

Fig. 8 HRTEM images of the composites milled for 40 h (a) and 60 h (b) after 5 cycles.

increasing after cycling.[43] A Si film anode introduced with SiO_x by annealing in air also showed considerably reduced crack in the electrode after cycling.[44] In the present study, in addition to the SiO_x, the $FeSi_y$ phases also contribute to the buffering of the volume expansion of the Si particles during lithiation.

As a micro/submicro-sized Si-based anode material, the present carbon-free Si@$FeSi_y$/SiO_x hybrid structures, especially those prepared after 60–80 h of milling, show extremely favorable rate-capability and cycle stability. The amorphous or nanocrystalline feature of the Si, the buffering of the amorphous SiO_x and the highly electrically conductive $FeSi_y$ ($FeSi_2$ and FeSi) phases play synergetic roles in generating the much superior electrochemical performance. Moreover, there is still large scope to improve further the electrochemical property of the Si@$FeSi_y$/SiO_x hybrid structure, such as using fine Fe powder, adjusting the ratio of Si and Fe, optimizing the milling time and using mixed gases of N_2 and H_2, to optimize the microstructure and phase composition of the hybrid structures. Furthermore, considering the facile and scalable fabrication method, the present Si-based material offers favourable potential for large-scale practical applications.

Conclusions

Particulate micro/submicro-Si@$FeSi_y$/SiO_x hybrid structures with a nanocrystallite and amorphous Si core coated by a diphase layer of amorphous SiO_x and nanocrystalline $FeSi_y$ ($FeSi_2$ and FeSi) are successfully synthesized by ammonia-assisted one-step planetary (low-energy) ball-milling of Si and Fe powder particles with a further rinse in a HCl solution to remove any residual Fe. $FeSi_2$ and FeSi phases are readily formed in an atmospheric environment of NH_3, which decomposes gradually to N_2 and H_2 during milling, whereas these are hardly formed under Ar atmosphere. The easy amorphism of Fe in the decomposed NH_3 is found to be the main factor for facilitating the formation of $FeSi_2$. The content of SiO_x is also strongly affected by the milling atmosphere. High levels of SiO_x (*ca.* 41–59 wt%) and a low level of FeSi (*ca.* 5 wt%) are obtained under the partial decomposition of NH_3. The level of SiO_x decreases to *ca.* 14–18 wt% and that of $FeSi_2$ increases to *ca.* 32–35 wt%, along with a certain amount of FeSi under a full decomposition of NH_3. The original crystalline Si particles change to a mixture of nanocrystallites and amorphous domains after the milling, especially upon a full decomposition of NH_3.

The introduction of the $FeSi_2$ and FeSi phases improves effectively the cycling stability and high-rate capability of the hybrid structures, due to the effective improvement of the electron conductivity and accommodation of the volume change of Si during cycling. The SiO_x contributes additionally to the cycle stability. The optimized hybrid structure possesses the highest capacity of 880 mA h g^{-1} at 100 mA g^{-1} after 150 cycles, corresponding to the capacity retention of 77%. A capacity of 560 mA h g^{-1} at 4000 mA g^{-1} is obtained. With consideration of the facile milling synthesis method and favorable electrochemical properties of the carbon-free Si@$FeSi_y$/SiO_x hybrid structures with micron and sub-micron sizes, the present Si-based material and its fabrication method offer great potential for large-scale manufacturing of cost-effective anode materials for Li-ion batteries in practical applications.

Acknowledgements

This work was supported by the National Natural Science Foundation of China (NSFC, nos 51371158 and 51201151), Program for "University Innovative Research Team" of the Ministry of Education of China (IRT13037), Pao Yu-Kong International Fund, Zhejiang University and EPSRC grant no. EP/K002252/1, UK.

Notes and references

1 M. N. Obrovac and L. Christensen, *Electrochem. Solid-State Lett.*, 2004, **7**, A93–A96.
2 Y. Wen, Y. J. Zhu, A. Langrock, A. Manivannan, S. H. Ehrman and C. S. Wang, *Small*, 2013, **9**, 2810–2816.
3 Y. F. Liu, R. J. Ma, Y. P. He, M. X. Gao and H. G. Pan, *Adv. Funct. Mater.*, 2014, **24**, 3944–3952.
4 K. Karki, E. Epstein, J. H. Cho, Z. Jia, T. Li, S. T. Picraux, C. S. Wang and J. Cumings, *Nano Lett.*, 2012, **12**, 1392–1397.
5 H. Wu, G. Chan, J. W. Choi, I. Ryu, Y. Yao, M. T. McDowell, S. W. Lee, A. Jackson, Y. Yang, L. Hu and Y. Cui, *Nat. Nanotechnol.*, 2012, **7**, 310–315.
6 K. Fu, Y. Lu, M. Dirican, C. Chen, M. Yanilmaz, Q. Shi, P. D. Bradford and X. W. Zhang, *Nanoscale*, 2014, **6**, 7489–7495.
7 S. L. Jing, H. Jiang, Y. J. Hu and C. Z. Li, *J. Mater. Chem. A*, 2014, **2**, 16360–16364.
8 B. Jerliu, L. Dorrer, E. Huger, G. Borchardt, R. Steitz, U. Geckle, V. Oberst, M. Bruns, O. Schneider and H. Schmidt, *Phys. Chem. Chem. Phys.*, 2013, **15**, 7777–7784.
9 S. Ohara, J. Suzuki, K. Sekine and T. Takamura, *J. Power Sources*, 2003, **119**, 591–596.
10 L. Y. Beaulieu, T. D. Hatchard, A. Bonakdarpour, M. D. Fleischauer and J. R. Dahn, *J. Electrochem. Soc.*, 2003, **150**, A1457–A1464.
11 P. Verma, P. Maire and P. Novak, *Electrochim. Acta*, 2010, **55**, 6332–6341.
12 K. W. Lim, J. I. Lee, J. Yang, Y. K. Kim, H. Y. Jeong, S. J. Park and H. S. Shin, *ACS Appl. Mater. Interfaces*, 2014, **6**, 6340–6345.
13 E. M. Lotfabad, P. Kalisvaart, A. Kohandehghan, K. Cui, M. Kupsta, B. Farbod and D. Mitlin, *J. Mater. Chem. A*, 2014, **2**, 2504–2516.
14 H. Park, S. Choi, S. J. Lee, G. Hwang, N. S. Choi and S. J. Park, *J. Mater. Chem. A*, 2015, **3**, 1325–1332.
15 P. Lv, H. Zhao, J. Wang, X. Liu, T. Zhang and Q. Xia, *J. Power Sources*, 2013, **237**, 291–294.
16 W. S. Chang, C. M. Park, J. H. Kim, Y. U. Kim, G. Jeong and H. J. Sohn, *Energy Environ. Sci.*, 2012, **5**, 6895–6899.
17 N. Yan, F. Wang, H. Zhong, Y. Li, Y. Wang, L. Hu and Q. Chen, *Sci. Rep.*, 2013, **3**, 1568.
18 H. Kim, M. Seo, M. H. Park and J. Cho, *Angew. Chem., Int. Ed.*, 2010, **49**, 2146–2149.

19 B. K. Guo, J. Shu, Z. X. Wang, H. Yang, L. H. Shi, Y. N. Liu and L. Q. Chen, *Electrochem. Commun.*, 2008, **10**, 1876–1878.

20 B. Philippe, R. Dedryvère, J. Allouche, F. Lindgren, M. Gorgoi, H. Rensmo, D. Gonbeau and K. Edstrom, *Chem. Mater.*, 2012, **24**, 1107–1115.

21 Y. S. Hu, R. Demir-Cakan, M. M. Titirici, J. O. Muller, R. Schlogl, M. Antonietti and J. Maier, *Angew. Chem., Int. Ed.*, 2008, **47**, 1645–1649.

22 Q. Sun, B. Zhang and Z. W. Fu, *Appl. Surf. Sci.*, 2008, **254**, 3774–3779.

23 F. Y. Cheng, J. Liang, Z. L. Tao and J. Chen, *Adv. Mater.*, 2011, **23**, 1695–1715.

24 R. Z. Hu, W. Sun, Y. L. Chen, M. Q. Zeng and M. Zhu, *J. Mater. Chem. A*, 2014, **2**, 9118–9125.

25 Y. Chen, J. Qian, Y. Cao, H. Yang and X. Ai, *ACS Appl. Mater. Interfaces*, 2012, **4**, 3753–3758.

26 S. Zhou, X. G. Yang, J. Xie, Z. I. Simpson and D. W. Wang, *Chem. Commun.*, 2013, **49**, 6470–6476.

27 H. J. Yu, K. P. Hong, M. S. Sung, S. Lee, K. Yoon Sheem and S. S. Kim, *ECS Electrochem. Lett.*, 2013, **2**, A10–A13.

28 S. B. Son, S. C. Kim, C. S. Kang, T. A. Yersak, Y. C. Kim, C. G. Lee, S. H. Moon, J. S. Cho, J. T. Moon, K. H. Oh and S. H. Lee, *Adv. Energy Mater.*, 2012, **2**, 1226–1231.

29 T. Li, Y. L. Cao, X. P. Ai and H. X. Yang, *J. Power Sources*, 2008, **184**, 473–476.

30 B. Lestriez, S. Desaever, J. Danet, P. Moreau, D. Plee and D. Guyomard, *Electrochem. Solid-State Lett.*, 2009, **12**, A76–A80.

31 A. L. Patterson, *Phys. Rev.*, 1939, **56**, 978–982.

32 D. S. Wang, M. X. Gao, H. G. Pan, J. H. Wang and Y. F. Liu, *J. Power Sources*, 2014, **256**, 190–199.

33 M. Gauthier, D. Mazouzi, D. Reyter, B. Lestriez, P. Moreau, D. Guyomard and L. Roue, *Energy Environ. Sci.*, 2013, **6**, 2145–2155.

34 K. A. Perrine, J. M. Lin and A. V. Teplyakov, *J. Phys. Chem. C*, 2012, **116**, 14431–14444.

35 V. Chirvony, A. Chyrvonaya, J. Ovejero, E. Matveeva, B. Goller, D. Kovalev, A. Huygens and P. Witte, *Adv. Mater.*, 2007, **19**, 2967–2972.

36 T. Kim, S. Park and S. M. Oh, *J. Electrochem. Soc.*, 2007, **154**, A1112–A1117.

37 B. C. Yu, T. Hwa, C. M. Park and H. J. Sohn, *J. Mater. Chem. A*, 2013, **1**, 4820–4825.

38 Y. Hwa, C. M. Park and H. J. Sohn, *J. Power Sources*, 2013, **222**, 129–134.

39 Y. Zhu, W. Liu, X. Zhang, J. He, J. Chen, Y. Wang and T. Cao, *Langmuir*, 2012, **29**, 744–749.

40 H. Kim and J. Cho, *Nano Lett.*, 2008, **8**, 3688–3691.

41 X. Huang, H. H. Pu, J. B. Chang, S. Cui, P. B. Hallac, J. W. Jiang, P. T. Hurley and J. H. Chen, *ACS Appl. Mater. Interfaces*, 2013, **5**, 11965–11970.

42 B. M. Bang, H. J. Kim, H. K. Song, J. Cho and S. Park, *Energy Environ. Sci.*, 2011, **12**, 5013–5019.

43 S. J. Sim, P. Oh, S. J. Park and J. Cho, *Adv. Mater.*, 2013, **25**, 4498–4530.

44 P. R. Abel, Y.-M. Lin, H. Celio, A. Heller and C. B. Mullins, *ACS Nano*, 2012, **6**, 12506–12516.